Geophys. J. Int. (2006) **164,** 425–440 doi: 10.1111/j.1365-246X.2005.02841.x

A tomographic image of Indian lithosphere break-off beneath the Pamir–Hindukush region

I. Koulakov[1,2] and S. V. Sobolev[1,3]

[1] *GeoForschungsZentrum Potsdam, Telegrafenberg,* 14473, *Potsdam, Germany. E-mail: ivan@gfz-potsdam.de*
[2] *Institute of Geology SB RAS, Novosibirsk, Russia*
[3] *Institute of Physics of the Earth, RAS, Moscow, Russia*

Accepted 2005 October 10. Received 2005 September 28; in original form 2004 December 8

SUMMARY

The *P* and *S* seismic anomalies in the upper mantle beneath the Pamir–Hindukush collision zone and surrounding areas are investigated using more than 4×10^5 traveltimes from 5775 events located in the study region, recorded by the stations of the worldwide seismic network and reported in the ISC catalogue. All available epicentral distance ranges of seismic rays are considered. All sources are relocated using an algorithm, which includes the double-difference method. In addition, source parameters are corrected in the main inversion step, simultaneously with the velocity models. The high reliability of the resulting *P*-velocity images is confirmed by various tests. The *S* model provides much smoother patterns, which are, however, generally consistent with *P* anomalies. Our model shows a complex image of lithospheric plate under the study region. Under SW Hindukush, the northwards subducting Indian plate is imaged throughout the upper mantle and transition zone. Further to the NE, within a 300-km-wide zone the upper part of the plate overturns and then the slab breaks off after it narrows at ∼250 km depth. The tomographic model also provides evidence for the southward subduction of the lithosphere beneath the southern Tien Shan down to at least 250 km depth. To the north of Tarim, we observe a northward-dipping of the Tarim plate down to ∼500 km depth. At the crustal depth our model shows alternating belts of high and low velocities parallel to the main thrusting faults, which indicate complex crustal structure in this region.

Key words: Hindukush, Pamir, slab break-off, seismic tomography.

1 INTRODUCTION

It is widely accepted that large-scale orogenic belts are associated with deformation processes in which both lithosphere and sublithospheric mantle may be involved. However, even major features of the lithospheric-scale strain partitioning in the orogenic belts are not completely understood so far. The Pamir–Hindukush region appears to assume a key position in the Alpine-Himalayan orogenic belt. Its complex tectonic structure, deep seismicity and numerous geophysical observations that are summarized in the next paragraphs, all suggest that it plays an important role in the intricate interaction of lithospheric plates beneath the Pamir–Hindukush region. However, the details of this process have remained unclear and contradictory, due in part to the spotty nature of the geophysical surveys. For example, some natural and political difficulties hamper the installation of a sufficient number of seismological stations that would facilitate the generation of a reliable high-resolution local tomographic model. The only way to retrieve the information about the mantle heterogeneities beneath this region is through the utilization of data for events located within the study region but recorded at global seismological stations located outside the study region. The main purpose of this study is to obtain the best possible tomographic image of the mantle beneath the Pamir–Hindukush using such data. In this study we present the algorithm of the inverse tomographic scheme (ITS), which performs an improved inversion for *P* and *S* velocities. We also provide some tests that prove the reliability of the obtained images. Finally, we present a short interpretation of the obtained results.

The Pamir–Hindukush is an orogenic area that is structurally controlled by large rigid lithospheric blocks: the Indian plate in the south, the Afghan block in the southwest, the Turan plate in northwest and the Tarim block in the northeast (Fig. 1) . Northward displacement of the Indian plate at a rate of 1–4 cm yr^{-1} (De Mets *et al.* 1994) results in strong compression of the interblock areas including the Pamir and Hindukush. On a regional level this compression causes a series of thrust belts such as the Gissal-Kokshal and the Darvaz-Karakul faults in central Hindukush, the Main Karakoram thrust fault in the middle and the Main Frontal thrust in the south (Fig. 1). However, location of these belts, as well as the direction of thrusting provided by various geologic investigations is often contradictory.

The ambiguity is related to the extremely complex structure of the crust, which has been strongly deformed at different stages of its evolution. The crust of the Pamir–Hindukush area was initially formed

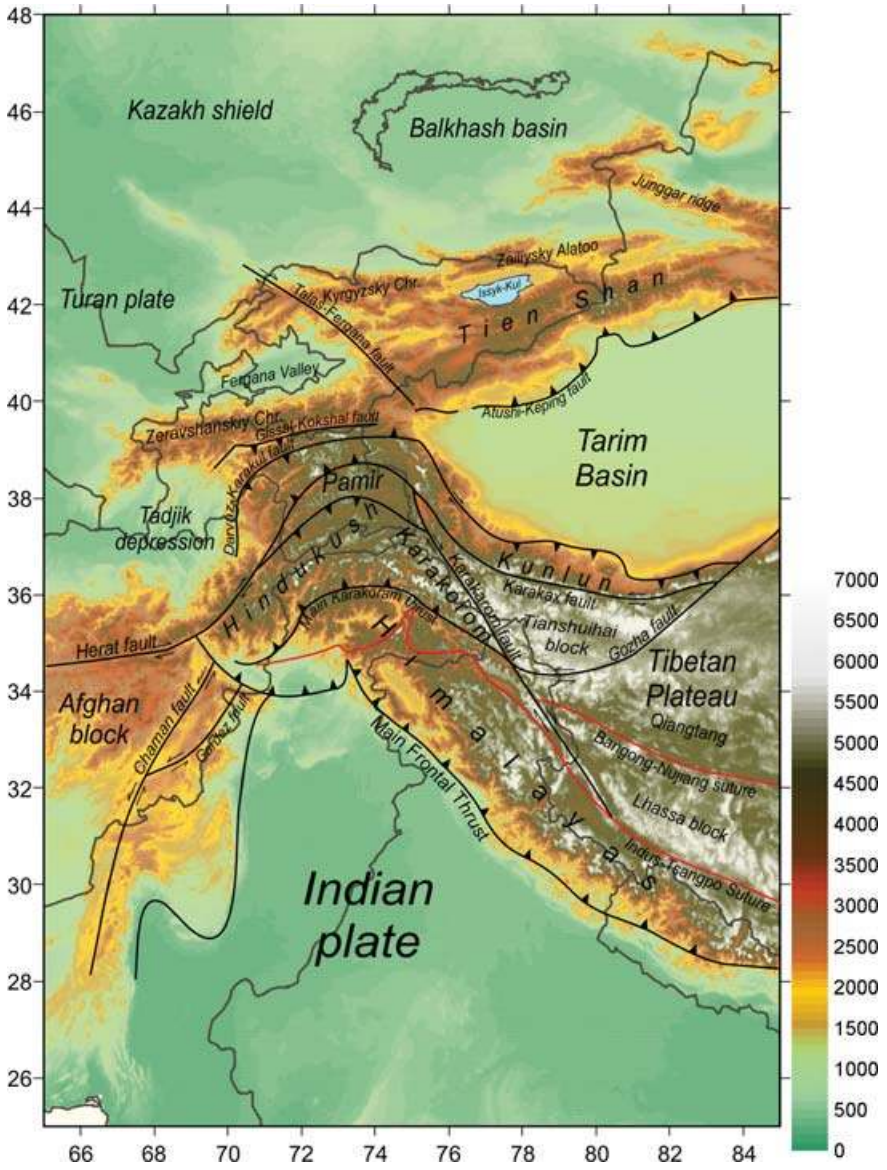

Figure 1. Relief and main tectonic features in the Pamir–Hindukush and surrounding areas, compiled from: (Zonenshain *et al.* 1990; Fan *et al.* 1994; Robinson *et al.* 2004; Wittlinger *et al.* 2004). Brown lines indicate political borders.

by the accretion of the palaeo- and neo-Tethys during the Triassic–Early Jurassic to Early Cretaceous times (Bazhenov & Burtman 1986; Zonenshain *et al.* 1990; Robinson *et al.* 2004). The collision of the Indian plate has resulted in strong crustal thickening. Surface wave tomography (Brandon & Romaniwicz 1986) and the interpretation of the gravity field (Molnar 1988; Burov *et al.* 1990) report a very large Moho depth in the Pamir, which reaches 70 km. For the calculation of traveltimes in our study, we use a smoothed $1^\circ \times 1^\circ$ crustal model (Fig. 8, later) (Laske, personal communication, 2004) that is constrained by the compilation of available Moho models in Eurasia (Beloussov *et al.* 1991; Li & Mooney 1998). According to this model, the crustal thickness in the study area varies significantly from 40 to 65 km.

The Pamir–Hindukush area is characterized by high concentrations of intermediate-depth earthquakes. These events trace the Wadati-Benioff zone, which dips to the north under the western and central parts of the Hindukush and southwards under the Pamir (Lukk & Vinnik 1975; Billington *et al.* 1977; Pegler & Das 1998). Microearthquake studies (Chatelin *et al.* 1980) in this region show seismicity extending to a depth of about 300 km. Two major tectonic models are suggested to explain the observed pattern of seismicity. One model suggests that two distinct slabs, the Indian and Asian slabs are subducted beneath the region with opposite directions (e.g. Chatelin *et al.* 1980; Roecker 1982; Burtman & Molnar 1993; Fan *et al.* 1994). The alternative model attributes the observed seismicity and mantle seismic structure in the region to only the northward subduction of the Indian plate, which overturns beneath the Pamir (Billington *et al.* 1977; Vinnik *et al.* 1977; Pegler & Das 1998; van der Voo *et al.* 1999; Pavlis & Das 2000).

Despite the geodynamic importance of the Pamir–Hindukush region, studies probing the deep structure of the area are generally sparse and contradictory. In particular, Roecker (1982) observes low seismic velocities in the upper mantle, from which he concludes partial subduction of the continental crust. Favouring this interpretation, many geological observations provide evidence for the underthrusting of the Eurasian continental lithosphere beneath

the Pamir (e.g. Hamburger *et al.* 1992). On the other hand, other studies based on teleseismic traveltime analysis (Lukk & Vinnik 1975; Vinnik *et al.* 1977) report faster seismic velocities associated with the Pamir–Hindukush seismic zone that suggest the possible subduction of mantle lithosphere. Similar features are observed in global tomographic models (Bijwaard *et al.* 1998; van der Voo *et al.* 1999; Bijwaard & Spakman 2000; Replumaz *et al.* 2004). According to these studies, under the Hindukush region in northeastern Afghanistan and southern Tajikistan, a northward-dipping slab is seen in the entire upper 600 km of the mantle and below. Farther to the east, under the Pamir, this same Indian slab shows a roll-over structure with the deeper portion overturned and dipping southwards (van der Voo *et al.* 1999). However, the global tomography studies cannot provide high-enough resolution of seismic structure, especially above 300 km.

Because of the unstable political situation, regional studies in this area are not currently possible. In recent times, the closest seismic network was located in Tajikistan, former USSR, which provided relatively good data for local seismicity. In fact, the territories of Tajikistan, as well as Afghanistan, are the 'white spots' for seismological observations. Therefore, the seismic events in the Pamir–Himalayas region are recorded today mostly from the southern azimuthal segment by seismic stations in Pakistan, India, Nepal, China and by the worldwide stations at teleseismic distances.

In this study, we explore the deep structure beneath the Pamir–Hindukush using a large amount of data accumulated in the catalogue of the International Seismological Center (ISC) (ISC 2001) and employing a tomographic inversion algorithm based on an idea of the ITS (Koulakov 1998; Koulakov *et al.* 2002). The ITS uses the principle of source–receiver reciprocity, which states that neither the path nor the traveltime of the seismic wave changes when source and receiver are interchanged. This means that in the tomographic inversion, a cluster of earthquakes in some seismically active region can be considered as an array of receivers, and vice versa, remote seismic stations that recorded those events, can be considered as teleseismic sources. In this scheme the existence of dense seismic networks is not required within a study area if there is a sufficient number of earthquakes recorded by the worldwide stations. The basic difficulty of the ITS is that the uncertainty of locations and origin times of the earthquakes may generate large errors in the inversion results. In this work we attempt to overcome this difficulty by inverting the traveltimes for origin times and locations of events, additionally to the seismic structure, using both the absolute location algorithm and the double-difference relocation algorithm (see Section 3.1). Further improvement of the previous algorithm (Koulakov 1998; Koulakov *et al.* 2002) is that in this work we use not only teleseismic rays but also the rays with small epicentral distances, including those with the distances less than 6°, reported by the Tajik seismological network. We also invert simultaneously for *P* and *S* velocities, and employ corrections for variable thickness of the crust and ellipticity of the Earth.

2 DATA

In this study the inversion is performed separately in three areas shown in Fig. 2 by circles, and then the results are combined into one map. All sources from the ISC catalogue for the period of 1964–2001, located within one of these three circles, with all available traveltime picks, are taken into consideration. Then, the rays having more than 50 records and maximal empty azimuthal sector (or GAP) less than 180° were selected. For the whole area we selected 5775 events recorded by 2435 stations (Fig. 3). Their relocated positions are shown in Fig. 2 and in the result section in vertical and horizontal slices (Figs 4–6). In total, arrival times of about 400 000 *P* rays and ∼46 000 *S* rays were selected. In addition 46 463 *pP* and 1162 *sS* phases were used to better constrain the depth of some sources. The distribution of epicentral distances in this data set is shown in the histogram in Fig. 7(a). Most of the short rays with distances less than 6° are reported by the Tajik seismological network, which was operating until 1990. The azimuthal coverage is plotted as a histogram in Fig. 7(b). An increased number of picks at ∼150° azimuth corresponds to the European stations, which provide an important part of data. Nevertheless we note, that azimuthal coverage of teleseismic rays in this study is favourable for high-quality tomographic inversion. As Fig. 3 shows, there are several significantly distinct directions (Europe, Japan, Alaska, Australia and South Africa), which provide a set of crossing rays. The readings from local distances (up to 6°) are used for source location and crustal investigations. The reported phases for greater distances are used primarily for velocity mapping of the upper mantle. The data corresponding to the rays at intermediate distances (6°–20°) are used to improve the vertical resolution of the model in the upper mantle, while the teleseismic rays are mostly responsible for constraining the horizontal position of seismic anomalies in the upper mantle.

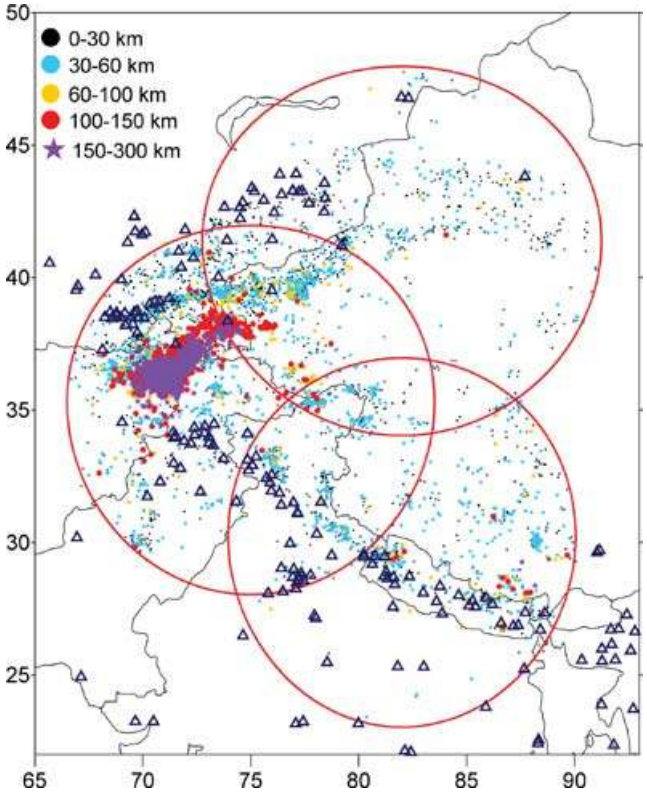

Figure 2. Distribution of relocated seismic sources used un this study. Colours of symbols indicate the depth range of hypocentres according to the scale in the left-top corner. The stations reported in the ISC catalogue are shown with triangles. Circles mark three areas in which the separate inversions are performed.

The basic ray parameters are computed using a 1-D spherical velocity model (here AK135 global velocity model, Kennett *et al.* 1995) with the Moho set at 50 km depth, based on the average crustal thickness in the Pamir–Hindukush. In the case of several ray paths between a source and a receiver, the first arrivals are considered.

Non-spherical terms related to variable Moho depth, surface topography and ellipticity of the Earth are added to the basic

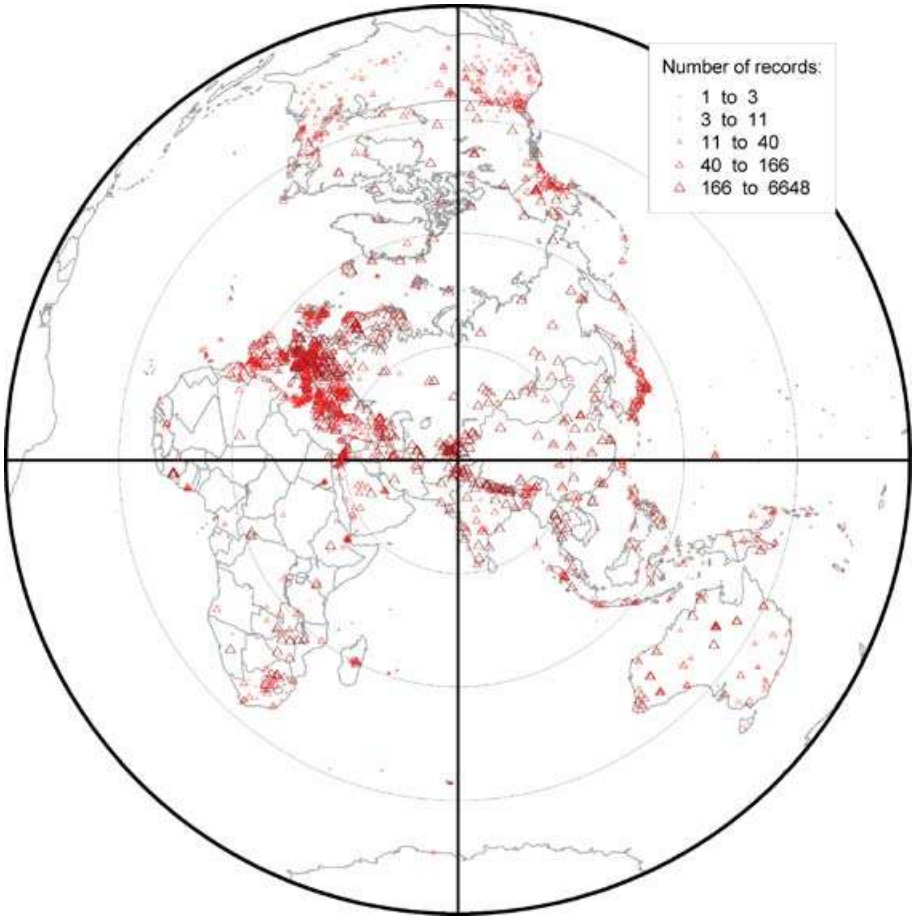

Figure 3. Distribution of stations from the ISC catalogue used in this study. The size of triangles indicates the number of picks from events in the Pamir–Hindukush area recorded at one station.

traveltimes, which are computed from the reference table corresponding to each source–receiver pair. If a source is located beneath the Moho, the correction for the crustal thickness variation is computed as follows:

$$dt^{\text{moho}} = dh\left|\sqrt{\sigma_1^2 - p^2} - \sqrt{\sigma_2^2 - p^2}\right|, \tag{1}$$

where σ_1, σ_2 are the values of slowness below and above the Moho interface, respectively, p is the ray parameter (horizontal component of the slowness vector) and dh is the difference between the Moho depth at the entry point and the average crustal thickness in the reference model.

For the head waves (refracted at the Moho) the correction for the Moho depth variation is computed using:

$$dt^{\text{moho}} = (dh_1 + dh_2)\sqrt{\sigma_1^2 - \sigma_2^2}, \tag{2}$$

where dh_1 and dh_2 are variations of the crustal thickness at the entry and exit points beneath the source and the receiver, respectively.

Moho depths at entry points are derived from a model of the crust with a resolution of $1^\circ \times 1^\circ$ (Fig. 8), which is available at the internet site: http://mahi.ucsd.edu/Gabi/rem.html (Laske, 2004, personal communication, 2004) for most parts of Eurasia and is a compilation of a number of models; Ziegler (1990), Blundell *et al.* (1992), Meissner *et al.* (1987), Seber *et al.* (1997), Beloussov *et al.* (1991), and Li & Mooney (1998). For the receivers located where no high-resolution data are available we use the model CRUST 2.0 (Bassin *et al.* 2000).

Correction for the topography is computed as:

$$dt^{\text{topo}} = dh\ \sqrt{\sigma^2 - p^2}, \tag{3}$$

where σ is the slowness in the uppermost layer and dh is the altitude of the station with respect to sea level.

3 METHOD

In this section, we describe the ITS, which uses phase readings from earthquakes in a region of interest, as reported by worldwide stations at all available distances. The use of source–receiver reciprocity allows tomographic studies of regions with sparse distribution of seismic stations, if the region has sufficient seismicity. This method was used earlier in (Koulakov 1998; Koulakov *et al.* 2002), but has since been significantly enhanced. In the current version, the method allows the relocation of events simultaneously with the determination of velocity perturbations in one inversion. Simultaneous inversion for source parameters and velocity models improves the reliability and resolution of the resulting model. This method allows investigation of any region with sufficient amount of the observed seismicity on a regular PC in a reasonable time frame.

3.1 Source location

As precise source locations are particularly important in the ITS, the locations listed in ISC bulletins have to be improved. Relocating the sources is performed in three steps:

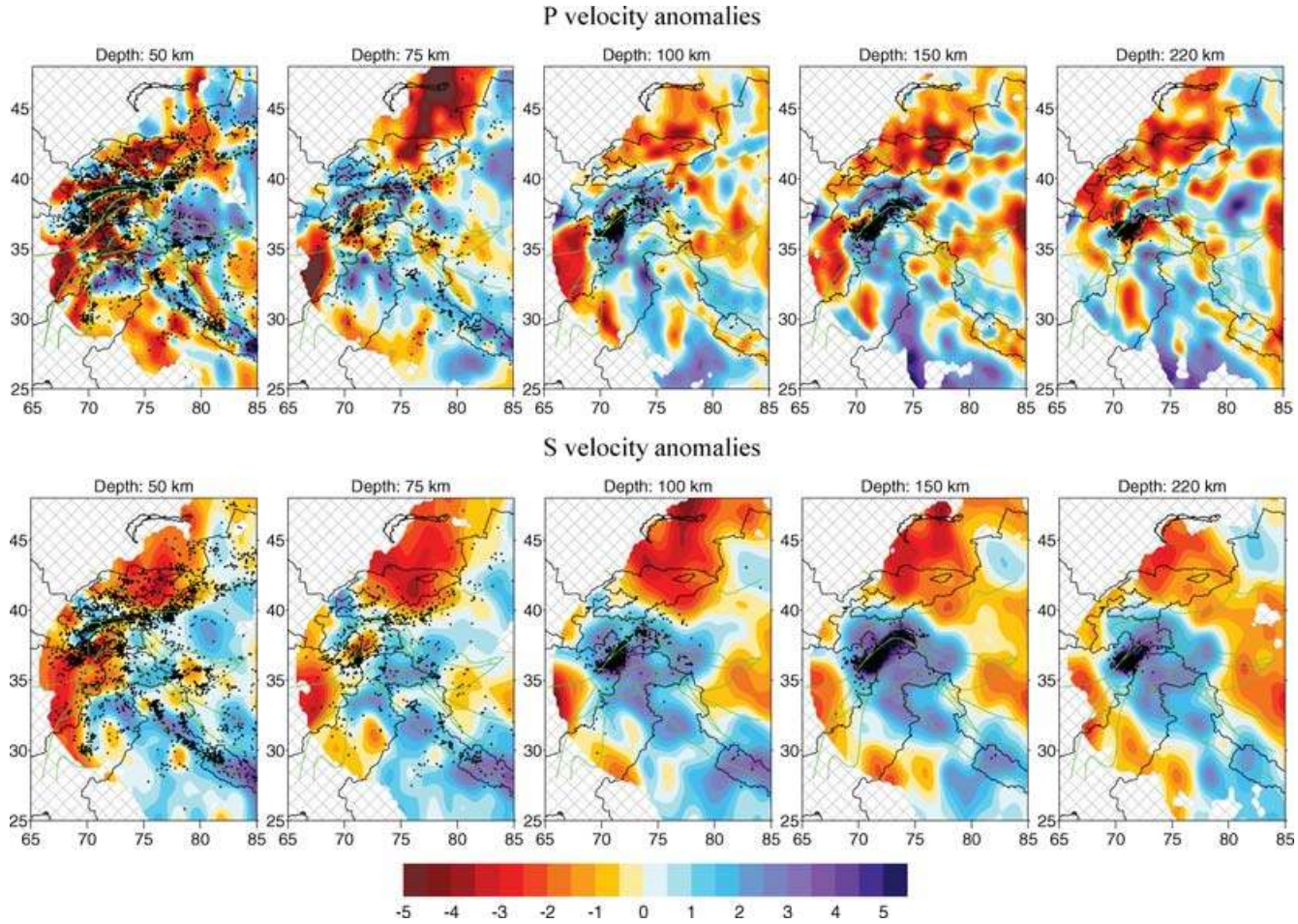

Figure 4. Horizontal sections of the resulting *P* and *S* velocity anomalies (upper and lower rows correspondingly) with respect to the average velocity models. Positions of the relocated sources at the corresponding depths are shown by black dots. Green lines show the main regional faults, the same as in Fig. 1. Positions of nine vertical sections presented in Fig. 5 are shown in the maps of 570 km depth.

(1) absolute location,

(2) adjustment of the source parameters using a double-difference scheme and

(3) recalculation of source parameters simultaneously with the determination of *P* and *S* velocity anomalies and station corrections in a general one-step inversion.

The details of the algorithm of absolute source location are given in the Appendix 1. This algorithm allows determination of the coordinates and origin times of the events from the ISC catalogue using some specialized distance weighting functions. In each point of the space we compute the probability function, which depends on amount of rejected 'bad' data and on the rms of the remaining residuals. The residuals are rejected if their values are greater than some predefined limit, which depends on the epicentral distance and phase (e.g. *S* residuals are allowed to be greater than *P* residuals). In such a way, the algorithm detects and rejects the outliers, which, according to our experience, take about 30 per cent of the initial ISC catalogue. The final position of a source is set in a point where the probability function is maximum that means minimum number of rejected phases and minimum rms of the remaining residuals.

Relative locations of events are adjusted using the double-difference method (Waldhauser & Ellsworth 2000). The main idea is based on the assumption that the residuals from two closely spaced sources recorded at a particular station should have similar values. The algorithm finds the coordinates and origin time corrections that minimize all possible double differences. We construct a linear system of equations for all combinations of source pairs (e.g. with numbers k and m), which are located at less than a predefined distance ($dS^{\max}$) apart from one another and having a common observation point i (the same station and the same *P* or *S* phase):

$$(P_x)_{ik}dx_k + (P_y)_{ik}dy_k + (P_x)_{ik}dy_k + dt_k^0 - (P_x)_{im}dx_m - (P_y)_{im}dy_m - (P_x)_{im}dy_m - dt_m^0 = dt_{ik}^{\text{obs}} - dt_{im}^{\text{obs}}. \quad (4)$$

We finally have a system of linear equations where the number of columns equals the number of sources, multiplied by four. Every row contains eight non-zero elements. For 1500 sources, the number of equations is about 1 000 000. This system can be inverted using the iterative LSQR method (van der Sluis & van der Vorst 1987). Following the inversion, the source parameters are updated and the procedure is repeated four to five times until it has converged.

3.2 Tomographic inversion

The general tomographic algorithm is based on a linear approach, where the ray paths are not updated with changes in the obtained velocity model. Parametrization of the velocity fields is performed on the basis of the algorithm developed in Koulakov (1998) and Koulakov *et al.* (2002). A certain amount of nodes is distributed within the study volume reflecting the density of rays. In this study

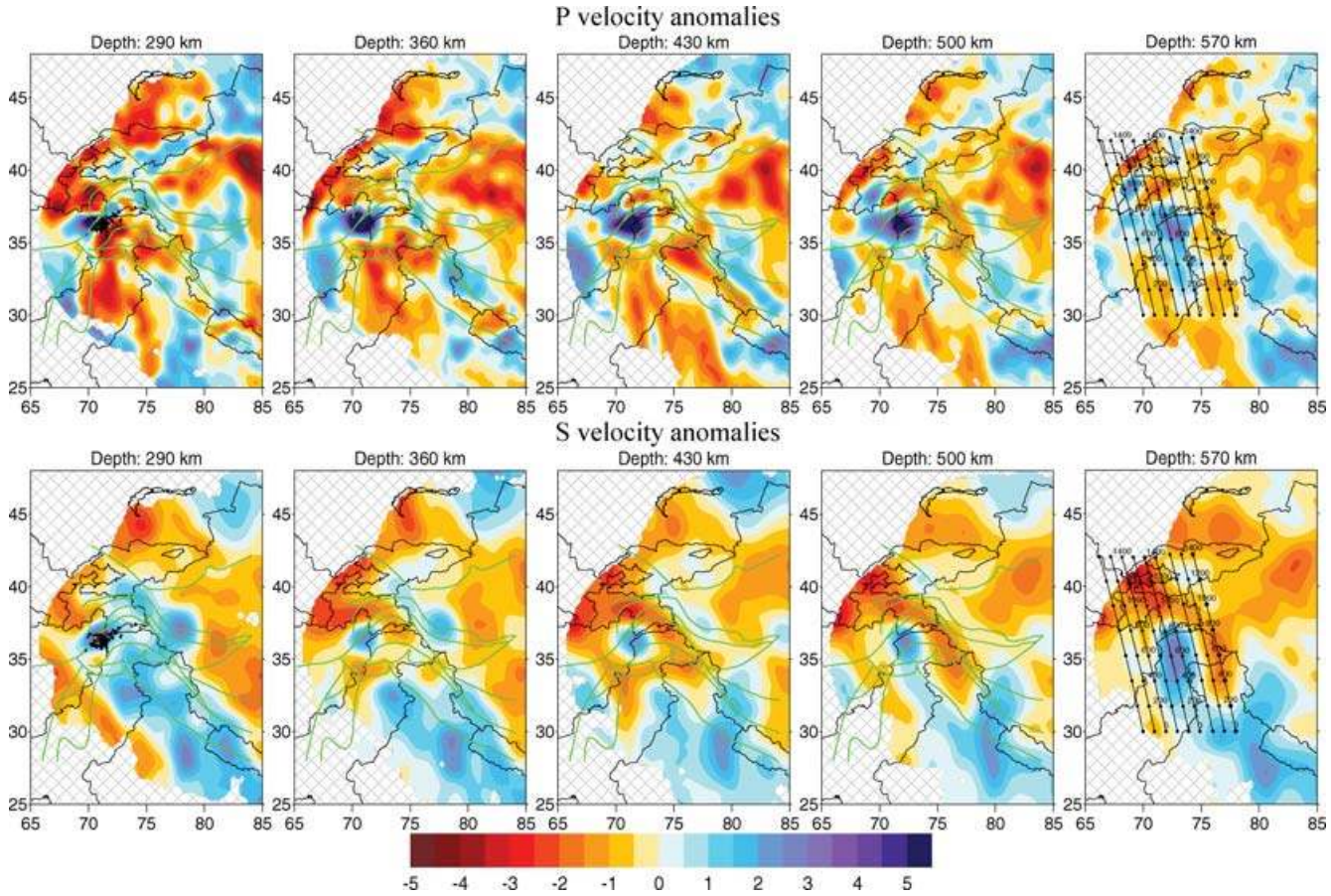

Figure 4. (*Continued.*)

the nodes are placed at 16 horizontal levels from 30 to 750 km depth. For each level a function of the ray density was computed, as shown in Fig. 9. The nodes are distributed on each plane along parallel lines proportional to the ray density. A minimal distance between nodes, ($dS^{\min}$) is set to avoid excessive concentrations of nodes in areas with density fluctuations. The nodes from adjacent depth levels are joined with each other and form a tetrahedral grid. Therefore, each point of the study volume is located inside one tetrahedron and is influenced by four nodes. The proposed parametrization method can potentially bias the resulting model due to the operator-induced orientations of the lines where the nodes are distributed. To avoid this problem we perform four separate inversions for four differently oriented grids: 0°, 45°, 90° and 135°. Summation of the resulting models removes most of the artefacts related to grid orientation.

The first derivative matrix A , which reflects the effect of velocity variations at the ith node on the traveltime of the jth ray, is computed by integration along the ray path γ as:

$$A_{ij} = \int_{\gamma} \Delta g_j(\gamma)\, dS/\Delta\sigma_j, \tag{5}$$

where Δg_j is a slowness perturbation at the current point of the ray caused by unit slowness anomaly $\Delta\sigma_j$ at the jth node. Together with the unknown P and S velocity anomalies, the matrix includes the elements for corrections of source parameters (four for each source) and station corrections.

Smoothing of the resulting velocity anomalies is controlled by an additional matrix block. Each line in this block contains two non-zero elements with opposite sign, corresponding to neighbouring nodes in the model. Increasing weights of these elements has a smoothing effect upon the resulting anomalies.

As a result, we get nine controlling coefficients responsible for different unknown parameters: $W1$ and $W2$ control 3-D P and S velocity anomalies; $W3$ and $W4$ control the P and S station corrections. $W5$, $W6$ and $W7$ are responsible for the horizontal and vertical shift of the sources and for the origin time; $W8$and $W9$control smoothing of the P and S velocity fields. Determination of all the coefficients in the matrix is a crucial and delicate problem. Pavlis & Booker (1980) suggest a method to separate different parameters and to perform the inversion independently. However, we suppose that in case of strong velocity anomalies as we expect in the study area, this method can cause some errors. In fact, P and S velocity parameters are linked with each other through the source parameters: change of one parameter affects the values of other parameters. Therefore, we believe that simultaneous inversion is more correct way. However, in this case there is a serious problem of definition of weighting coefficients for different sorts of parameters. These coefficients depend on the expected amplitudes of the parameters, but also on quality and amount of data, number of parameters, specific features of the observation system, etc. Total formalization of the weighting definition seems to be not possible. In our practice, we define the coefficients using the results of synthetic tests with realistic values of parameters and noise level.

The resulting matrix is inverted using the LSQR method (Paige & Saunders 1982; van der Sluis & van der Vorst 1987). The number of LSQR iterations providing a satisfactory convergence in our case

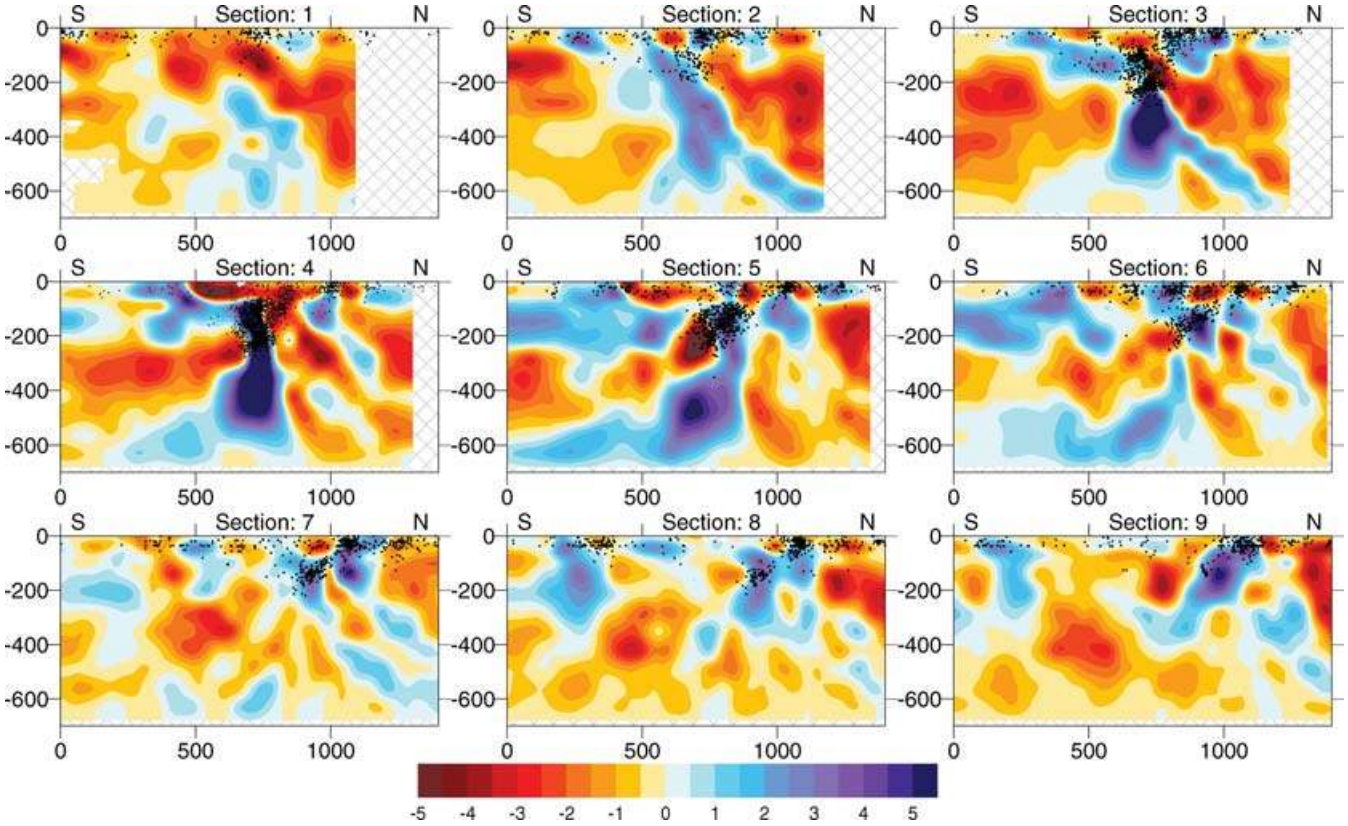

Figure 5. Vertical sections of the resulting *P* velocity anomalies in the Pamir–Hindukush regions with respect to the average velocity models. The relocated events, that are within 40 km of each profile, are shown by black dots. Positions of the sections are shown in Fig. 4 in the maps of 570 km depth.

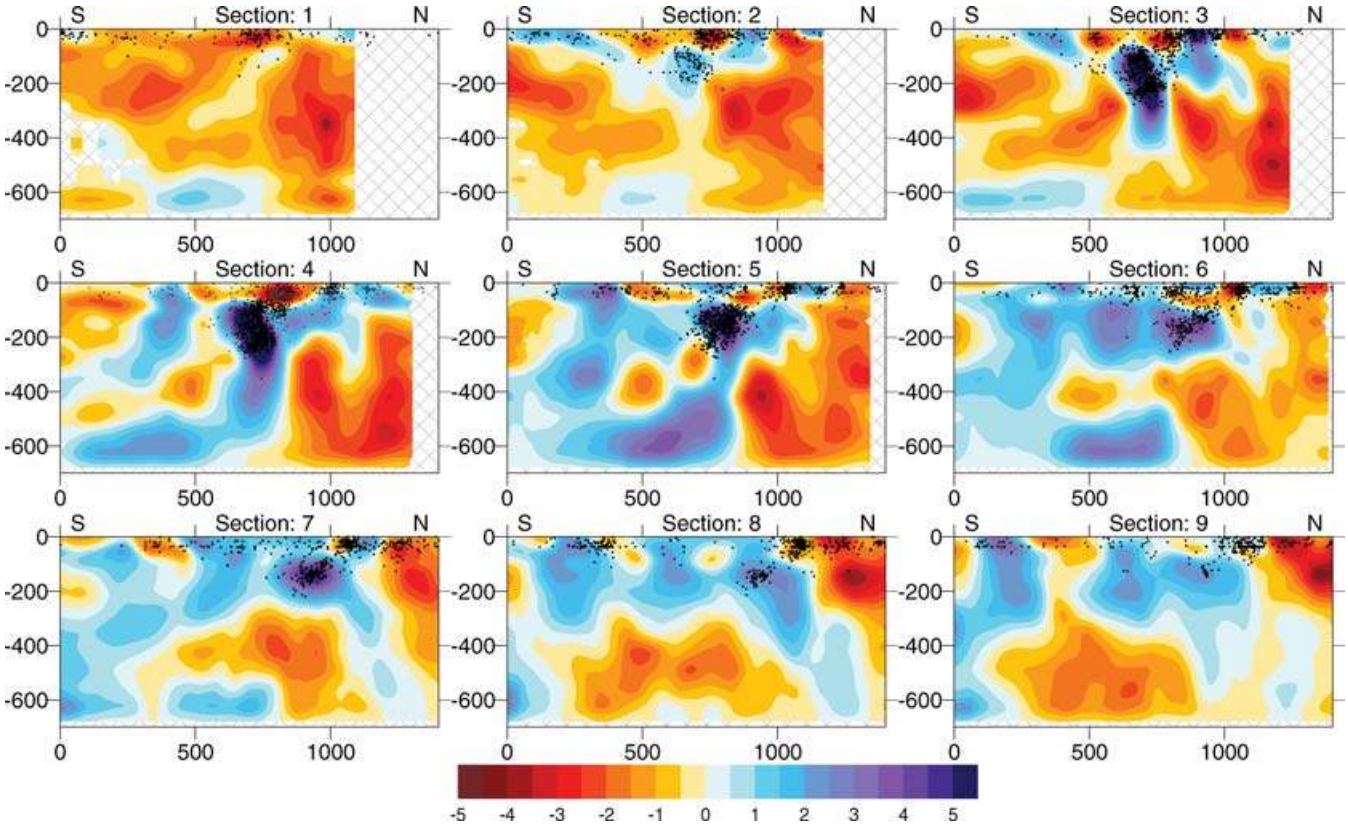

Figure 6. Same as Fig. 5, but for the *S*-velocity anomalies.

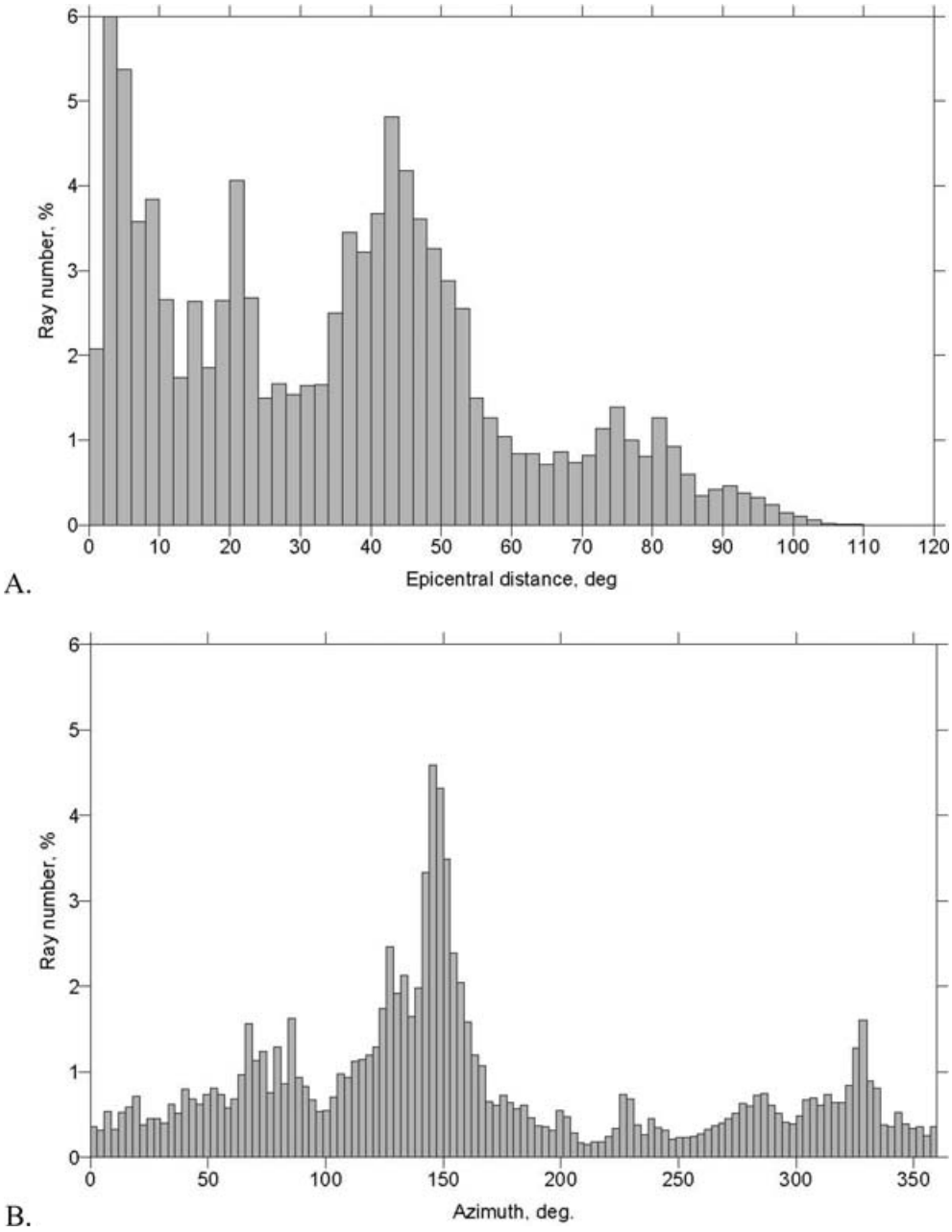

Figure 7. Histograms of data distribution according to epicentral distance (a) and azimuth (b).

is 50. The variance reduction for *P* residual times is ∼50 per cent, while for *S* data it is only ∼30 per cent. This fact can be explained by significantly higher noise levels in *S* times.

As in Koulakov *et al.* (2002), the entire study area is divided into a number of smaller overlapping regions (Fig. 2). The inversion is performed independently in each region, and the results are added and averaged. There are several reasons for such a step-by-step inversion. First of all, the calculations are done in Cartesian coordinates and, if the area is too large, the transformation of geographical to Cartesian coordinates causes significant errors. In addition, comparison of the results in the overlapping areas is another test to check the stability of the inversion. In particular, if an anomaly is located near the margin of one of the regions, we can check the neighbouring regions and see if the anomaly is significant, or if it is a marginal artefact. Furthermore, overlapping of neighbouring regions has a smoothing effect on the results and helps to stabilize the inversion.

In this work we divide the study area into three overlapping blocks. For each block the velocity model is the mean value of four different grid orientations. The final model is, therefore, obtained as the average of 12 separate models. The summary velocity model is computed as:

$$dV^{\mathrm{sum}} = \sum_{i=1}^{12} C(d^{\mathrm{cen}}) D(d^{\mathrm{node}})\, dV_i \Big/ \sum_{i=1}^{12} C(d^{\mathrm{cen}}) D(d^{\mathrm{node}}), \qquad (6)$$

where C is a function depending on the distance from the centre of the current model (for distances up to R/2, where R is the radius of the current area, $C = 1$; for distances from $R/2$ to R the value of C

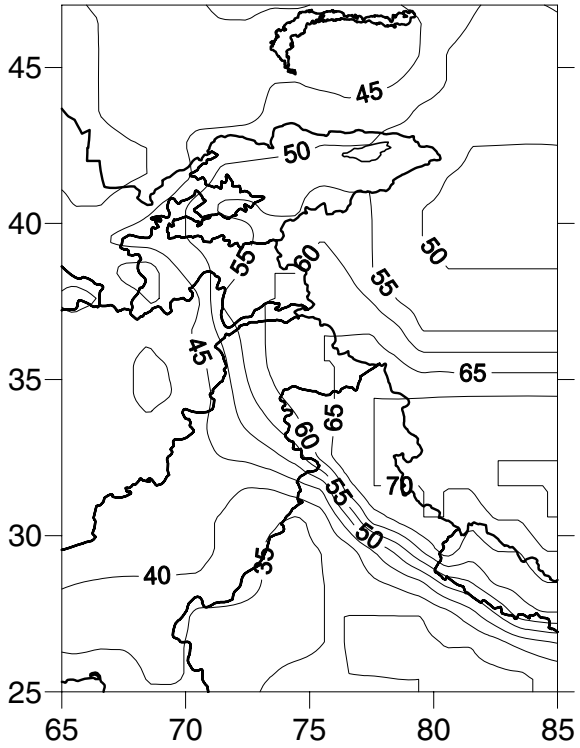

Figure 8. Moho depth in model CRUST2.0 (Bassin *et al.* 2000; Laske, personal communication, 2004) updated with the 1° × 1° model (Laske, personal communication, 2004).

decreases linearly from 1 to 0); D depends on distance to the nearest parametrization node. The values of the velocity anomalies are given only if the distance to the nearest node is less than a predefined value $d^{\min}$ (40 km, in our case).

4 RESULTS

4.1 Results of data inversion

P and *S* velocity anomalies beneath the Pamir–Hindukush and surrounding areas, together with the position of relocated sources, are presented in horizontal and vertical sections in Figs 4–6. Red colours indicate low-velocity anomalies, which can be interpreted as regions with elevated temperature as it was found in other regions (e.g. Sobolev *et al.* 1996, 1997). The reliability of the obtained results is checked with a series of different tests described in the next sections. In particular, we can see from the resolution test (Section 4.3) and inversion of two data subsets (Section 4.2) that the reliability of the *S* model is significantly lower than that of the *P* model, due to the lower number of *S* picks and their significantly lower accuracy. To eliminate instabilities related to the noise, we have to use 10 times larger damping parameters for inversion for *S* models than for *P* models. Consequently, the *S* model appears to be much smoother than the *P* model.

We present the results starting from 50 km depth, just above the Moho. We are not able to investigate shallower structures. Our data set is mostly based on teleseismic and regional rays for which there is a trade-off between the depth of crustal events and crustal velocities, and thus there is no resolution for crustal velocities.

The horizontal and vertical sections (Figs 4–6) show several interesting features. At the depths of 50 km, several elongated alternating high- and low-velocity anomalies, oriented subparallel to the

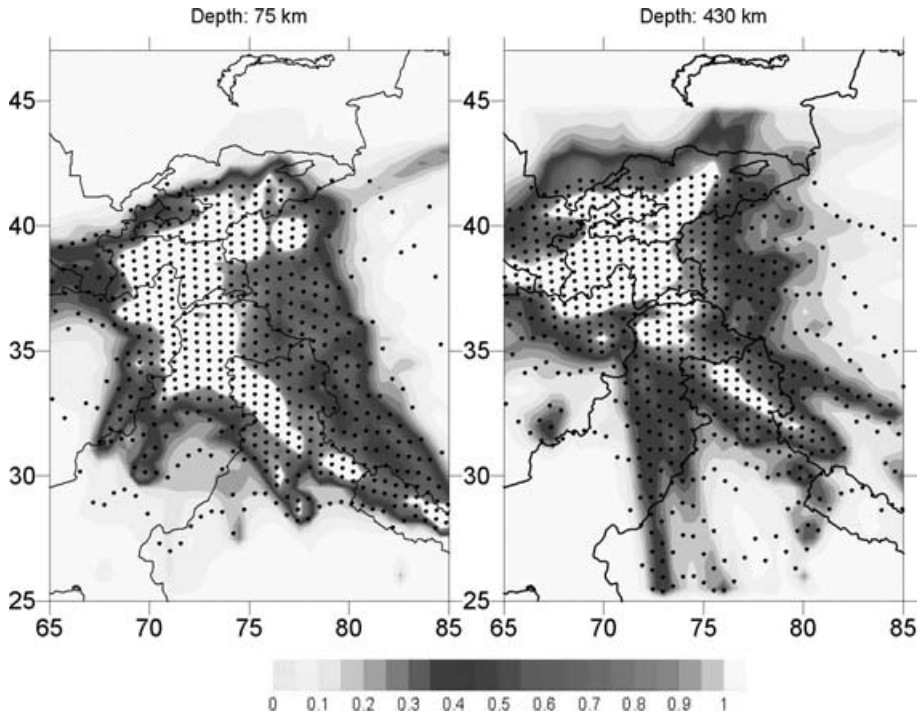

Figure 9. Examples of grid construction at two depth levels. Contour lines show the ray density in relative units. Dots indicate the position of the parametrization nodes.

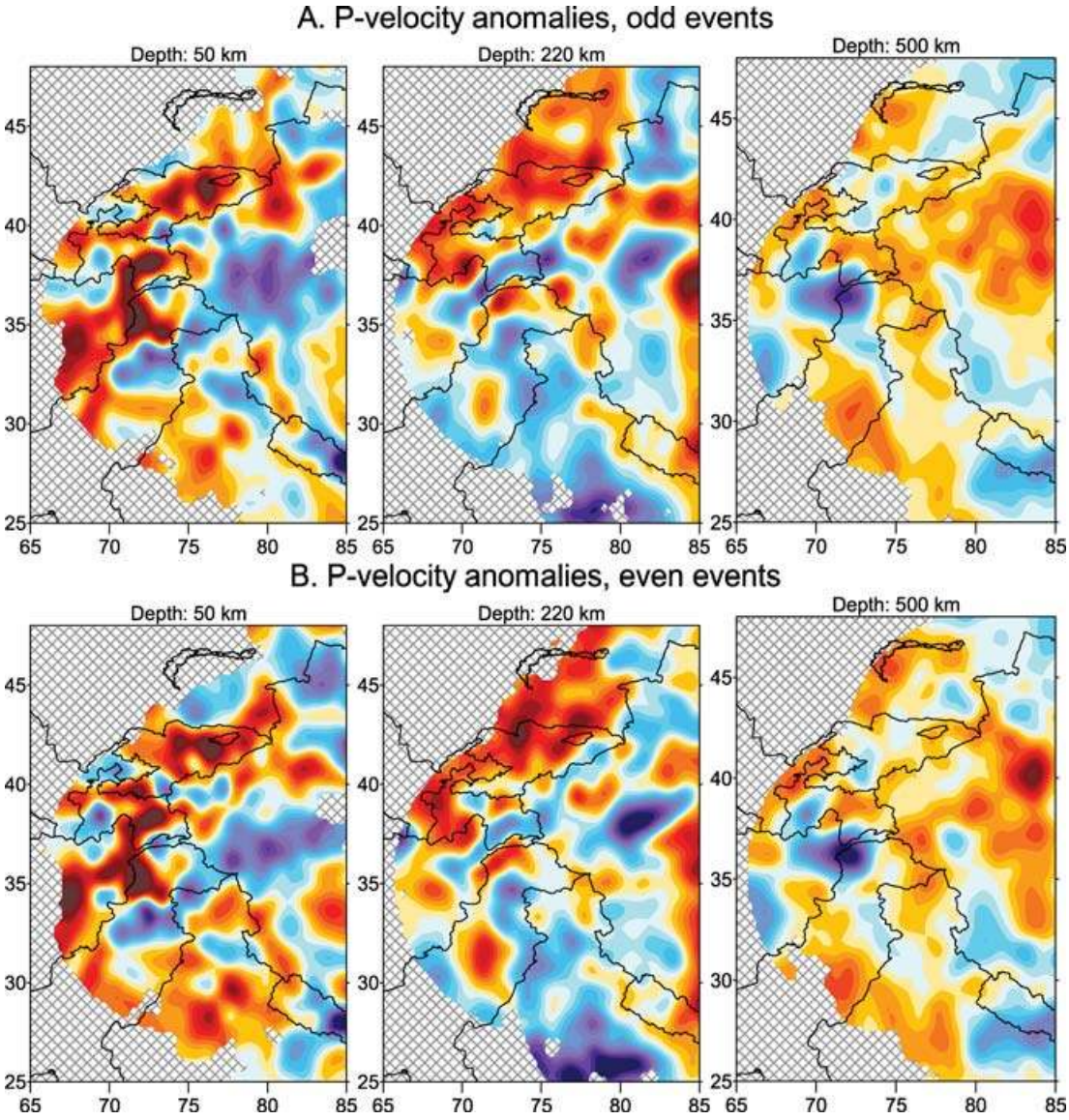

Figure 10. Result of inversion of two independent subsets of data. (a) *P*-velocity anomalies, odd events; (b) *P*-velocity anomalies, even events; (c) *S*-velocity anomalies, odd events and (d) *S*-velocity anomalies, even events.

major thrust faults, are observed in the central part of the study area. The strongest high-velocity anomaly in the crust is observed along the northern thrust zone from the Tajik depression in the west to the Tarim block in the east, which could probably indicate remnants of the oceanic crust. This belt is surrounded by the Gissal-Kokshal and Darvaz-Karakul thrust faults and coincides with a maximum in crustal seismicity. To the south, a low-velocity block under the Pamir is located in a divergent area between oppositely oriented thrust belts. This low-velocity anomaly, observed both in *P* and *S* models down to significant depths (at least to 100 km depth), probably indicates the continental crust entrained into the upper mantle by the subducted Indian plate. Apparently this anomaly was observed by Roecker (1982) who, based on this observation, suggested partial subduction of low-velocity continental crust. At a depth of 150 km this anomaly almost disappears.

In the N–W corner of the study area, the alternation of mountain ridges and depressions is apparent in the shallowest tomographic sections. The Tajik depression, Fergana valley, Balkhash basin are marked by high velocities in the crust, while the mountain ridges Zeravshanskiy and Kyrgyzsky coincide with low-velocity anomalies. The correlation of seismic velocities at the depth of average Moho with the main topographic features can be explained by Moho depth variations that were unaccounted for in the starting model. However, we do not have sufficient grounds to quantify this hypothesis.

Another system of linear structures is observed in the western Himalayas, in the southeastern part of the study area. The linear anomalies there are consistent with the orientation of the main sutures and thrust belts. The Main Frontal Thrust (limit between India and Himalayas) lies just on a transition between a low-velocity block to the south and a high-velocity belt to the south. The Karakarom fault coincides with an elongated low-velocity anomaly. The eastern edge of the Tibetan plateau is marked by low-velocity anomalies. The alternation of high- and low-velocity blocks indicates complex structure of the crust in this area that has been accreted during old and recent periods of Indian plate collision.

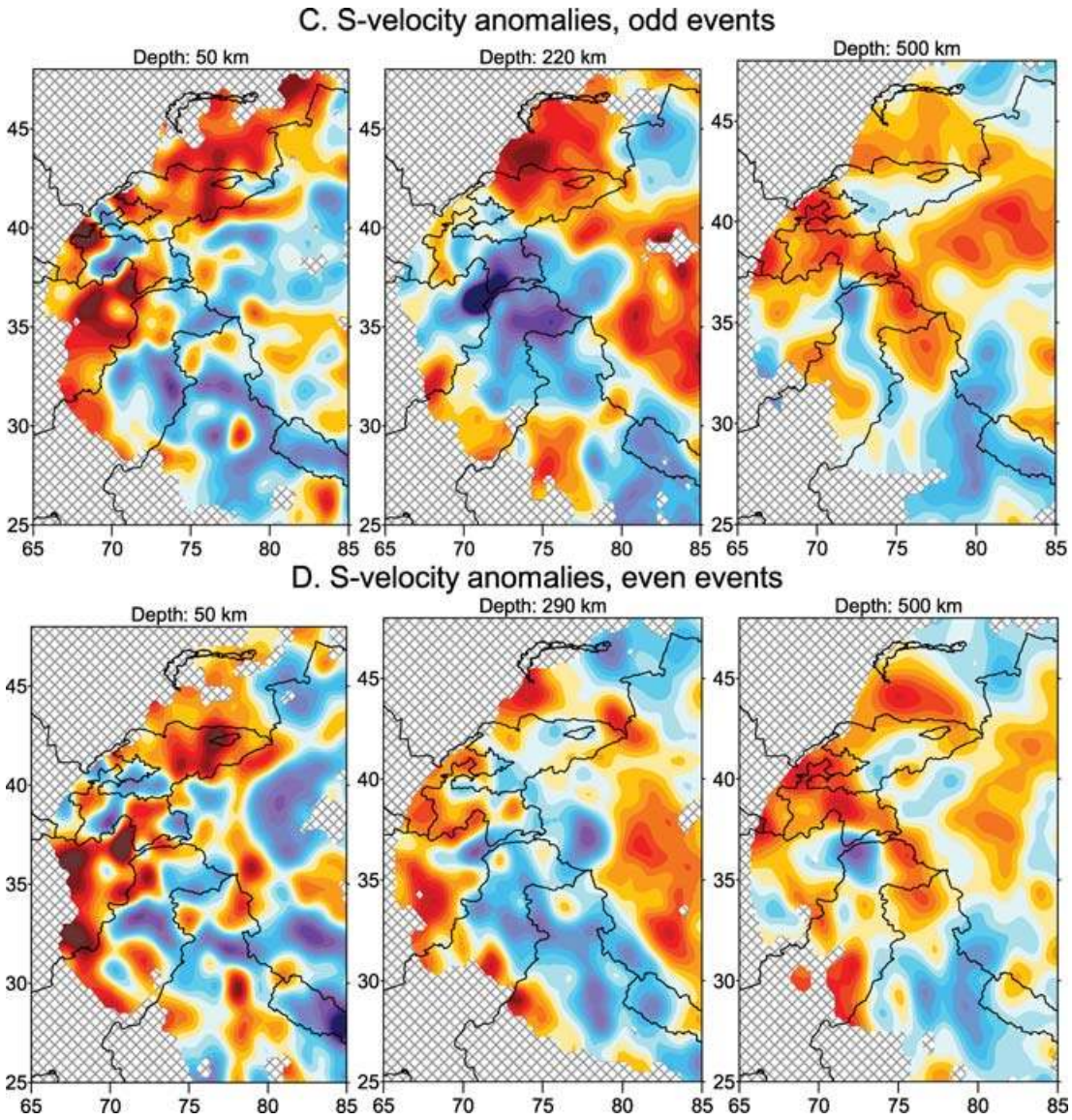

Figure 10. (*Continued.*)

The sections at 150, 220 and 290 km depth roughly show the relief of the lithosphere–asthenosphere boundary. In particular, judging from prominent high-velocity anomalies at these depths, the Indian lithosphere appears to be rather thick compared to the lithosphere of the Afghan block and the Kazakh shield beneath the Balkhash basin. Beneath the Tarim block a high velocity at 220 km depth is replaced with low velocities at deeper sections. This transition gives an estimate for the lithosphere thickness under Tarim of about 250 km. To the north of Tarim, we observe a linear high-velocity pattern, which is similarly shaped as the Atushi-Keping fault and gradually deepens northwards to a depth of at least 500 km. To all appearance, this anomaly indicates the northward subduction of the Tarim lithosphere. Another positive anomaly, which can be interpreted as the trace of the subducted lithosphere is located beneath the Lhassa block, in the western Himalayas, which is observed in all depth ranges both in the *P* and *S* models.

However, the most interesting feature of this model is the image of the subducted slab in the Pamir and Hindukush. This slab is clearly seen in the horizontal sections (Fig. 4) at depths from 200 to 570 km. Its shape can be seen most clearly in vertical sections (Figs 5 and 6). Scanning through the sections from SW to NE, one can observe different stages of the subduction development. In Section 1 the slab is not well visible. The slab image is becoming clearer to the east, in Sections 2–4, where the northward-dipping plate (Indian lithosphere?) is continuously imaged at least down to the bottom of the mantle transition zone. The contact zone between the subducted Indian and overriding Asian plates is clearly seen in these cross-sections and is marked with a salient cluster of earthquakes observed down to 250 km. In these sections, earthquake clusters are mostly located in the domains with highest seismic velocities. Just above the high-velocity domain marked by the earthquake cluster in Sections 3 and 4, there is a low-velocity anomaly. It can be interpreted as low-density crustal material entrained by the subducted mantle lithosphere. In Sections 4 and 5 where the deep seismicity reaches its maximum, the direction of subduction is not as clear as in Section 3. However, joint interpretation of all these sections suggests that the same plate gradually overturns and rotates. This overturn continues in Section 5, which could be interpreted

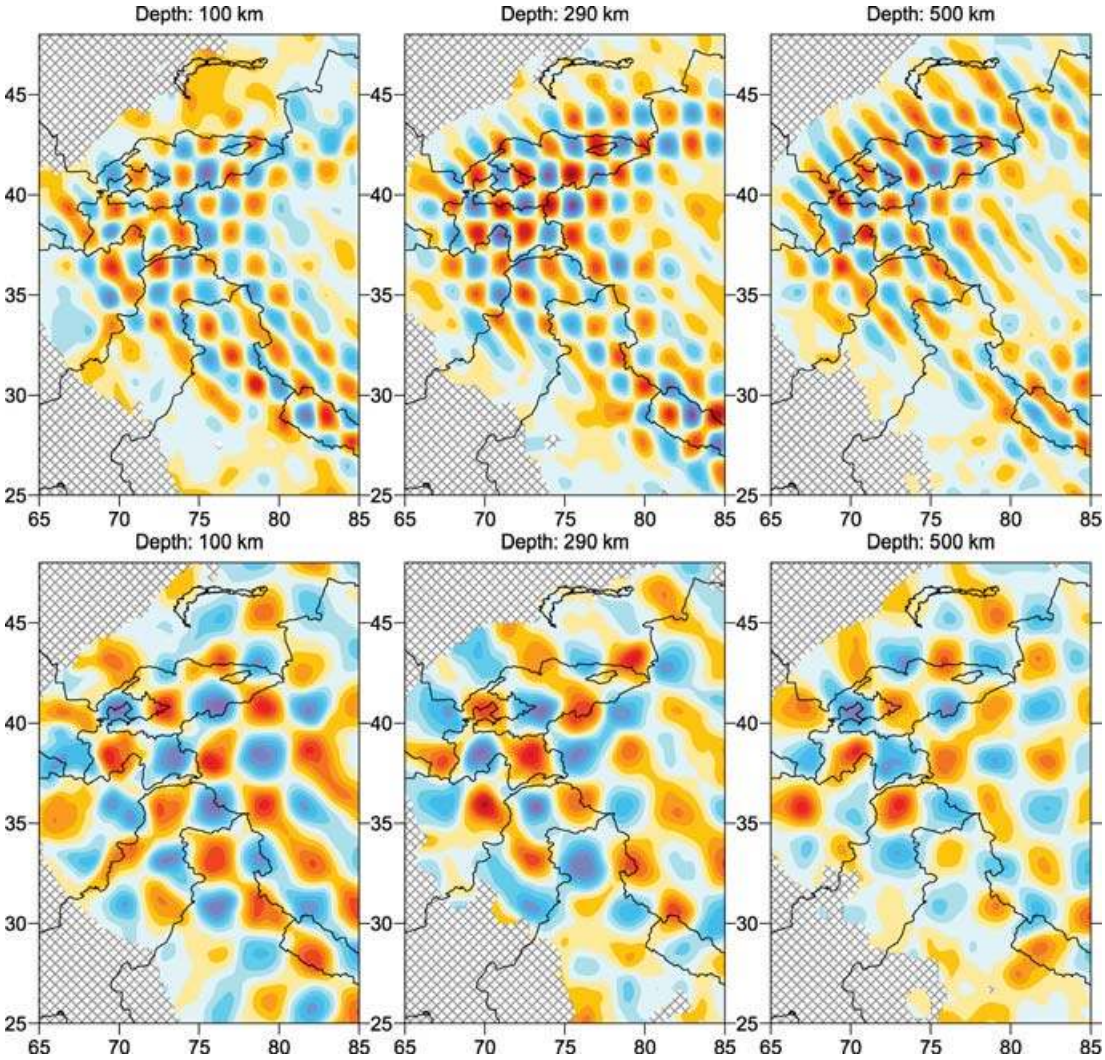

Figure 11. Results of the reconstruction of chessboard anomalies using the actual ray configuration. Upper row is the result for *P* model recovering at three depth levels, lower row is the same for *S* model. Descriptions of the initial velocity anomalies, parameters of noise and details of the algorithm are given in the text. The colour scale is the same as in Fig. 4.

otherwise as an image of the southward-subducting slab if Sections 3 and 4 were not considered. Sections 4 and 5 also indicate a thinning of the subducting slab at a depth of ∼200 km, which looks like a gradually developing slab break-off. Resolution tests, shown in the next section, confirm the accuracy of the tomographic images which motivate our interpretations, such as thinning of the high-velocity anomalies and moving of the velocity maximum downwards. Just 100 km east of the 'developing break-off', Sections 4 and 5 and farther to the east, there is no more slab penetrating through the asthenosphere (Section 6), although high-velocity material is present deeper than 300 km. This may indicate that the slab break-off has already occurred in the region imaged from Section 6 and further east.

At the same time, in the southern parts of the Sections 4–9, beneath the southern Tien Shan, we notice the presence of another high-velocity body, which has a tendency of dipping down southwards to 300 km depth. The position of high-velocity anomalies matches the distribution of deep seismicity, which in Sections 6–9 has the shape of inclined Benioff zone down to the depth of 200 km. Note that the maximal seismicity and the point of break-off of the Indian plate (Section 5) coincide with the place where the Tien Shan plate touches the Indian plate. This could indicate that this plate plays a major role in the break-off of the Indian plate.

4.2 Test with odd and even numbers of events

The contribution of random noise to the resulting images can be estimated by performing independent inversions for independent data subsets. In this test, we divide the whole data set into two subsets: with odd and even numbers of events. The structure of the processing algorithm is the same as in the case of inverting of the entire data set. All tuning parameters remain the same, with exception of smoothing coefficients $W8$ and $W9$, which are two times smaller for the halved data sets.

Results of inversion for *P* and *S* models are shown in Fig. 10. The models can be compared with each other and also with the results using the entire data set (Fig. 4) to show the effect of data halving on the inversion results. Separate inversions for the *P* model (plots A and B) show almost perfect correlation between the maps at corresponding depths. Even small patterns, less than 100 km of lateral size, are reliably reconstructed in all maps. This gives us

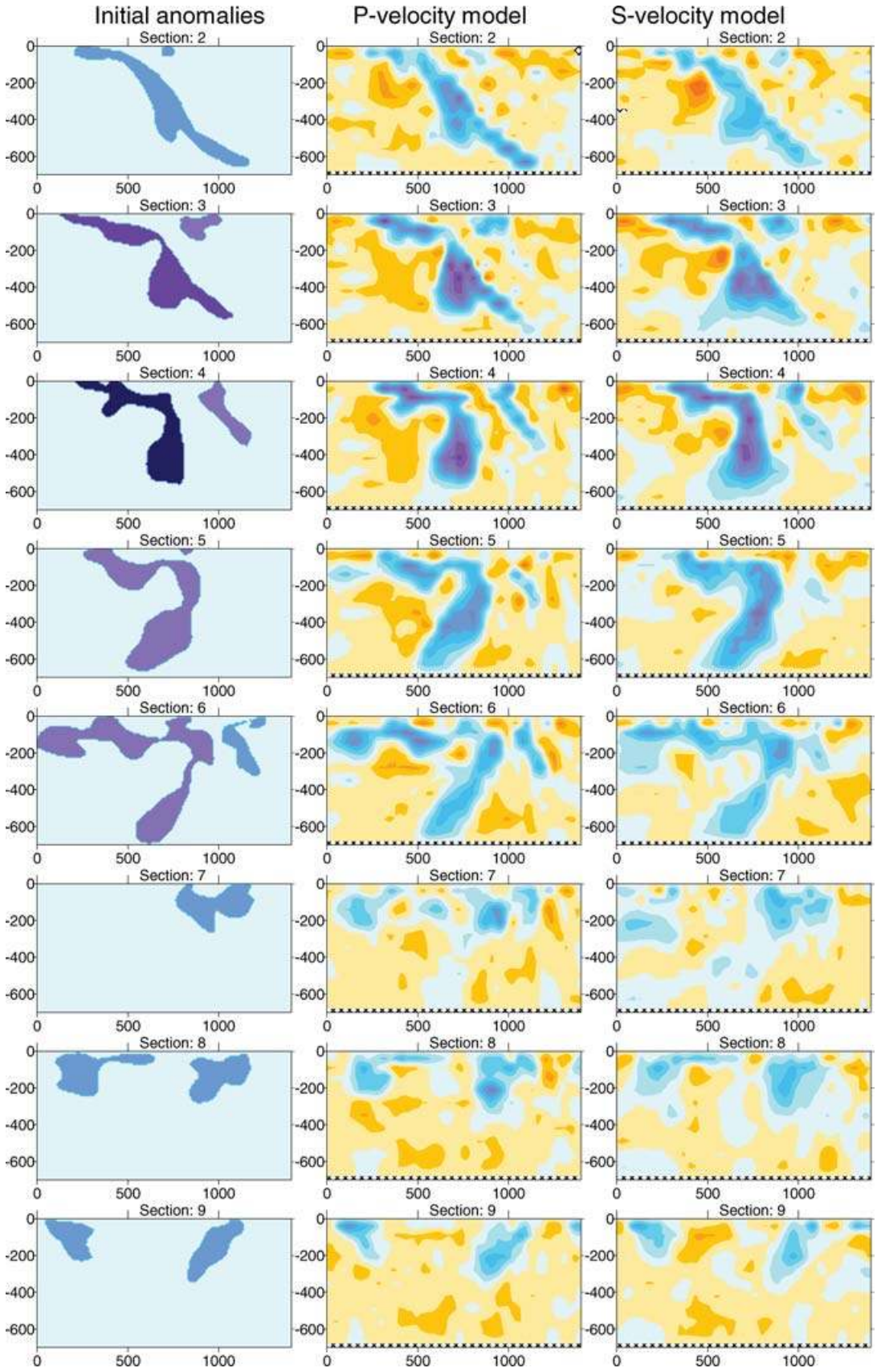

Figure 12. Reconstruction of synthetic slab-shaped anomalies in nine vertical sections. The left column shows the initial shape of anomalies, and the results of the inversion are shown in the middle (*P* model) and right (*S* model) columns. The position of the sections is the same as for the real data inversion (Figs 5 and 6). Parameters of noise and details of the testing algorithm are described in the text. The colour scale is the same as in the Fig. 4.

quite high confidence to the obtained *P* velocity model. Results of the *S* model (Figs 10c and d) are much poorer. Only long-wavelength features with a dimension of more than 300 km are resolved reliably in all maps. The smaller anomalies in many cases do not match each other which may indicate that they can be produced by random noise in the initial *S* data. To achieve a satisfactory fit of the *S* anomalies in this test, we have to use fairly large values of the smoothing parameters to get rid of the noise related anomalies.

4.3 Sensitivity tests and synthetics

We focused special attention on the problem of testing the reliability of the inversion. The resolving power of the algorithm, including its stability against noise in the data, is tested in a series of synthetic tests. We define a synthetic model of 3-D velocity anomalies in the study area. The synthetic time residuals are computed along the same rays as in the data set. Delays related to the 3-D velocity anomalies are integrated along the path of an arbitrary ray, γ, according to:

$$dt^{\mathrm{vel}} = -\int_{\gamma} \frac{0.01\, dv(\mathrm{per\ cent})}{V_0}\, ds. \tag{7}$$

The 'observed' traveltimes (T_{obs}) for the synthetic test are computed as the sum of the traveltimes in a reference model (T_{ref}), synthetic delays (dt_{vel}), and a random noise ε:

$$T_{\mathrm{obs}} = T_{\mathrm{ref}} + dt_{\mathrm{vel}} + \varepsilon. \tag{8}$$

Noise is produced by a random numbers generator with a predefined distribution, that is similar to the histogram of real ISC delays. The amplitude of the noise is set to reach a predefined value for the standard deviation. In addition, the noise generator algorithm allows adding outliers to the data set. In this study, the noise for 10 per cent of the data is multiplied by 10. This roughly reflects the state of the ISC data. The times computed in [13] are used as the input data for the complete inversion procedure. Unlike most tomographic studies which only invert the synthetic residuals, our tests start from the step of absolute source location using absolute arrival times. To achieve an unbiased comparison, the inversion parameters for the synthetic test are the same as those used in the real data processing.

In the first test, the horizontal resolution of the model in the upper mantle is checked. We show here the results of chessboard tests, where input heterogeneities of alternating sign (±3 per cent) are superimposed on the average velocity distribution. The anomalies are defined in cells (1° for *P* model and 2° for *S* model) and spaced apart by the areas with zero values. Lateral periodicity of anomalies ('0' - '+3' - '0' - '−3') is defined at 3° for *P* model and at 6° for *S* model. The sign of anomalies is changed every 200 km depth (e.g. 200, 400, 600 km).

The result of the reconstruction is shown in Fig. 11. The value for the standard deviation of the noise without outliers is 0.5 s. The standard deviation of the summary synthetic residuals with outliers is 0.95 s. For comparison, the standard deviation of the synthetic residuals is only 0.44, that is, more than two times smaller than the noise level. Inversion with this noise level provides 48 per cent variance reduction, similar to the value observed in the real data inversion. The result of reconstruction (Fig. 11) shows that even with the exaggerated level of the noise used here, the main patterns are reconstructed correctly, except for some smoothing and reduction in amplitude.

The second test (Fig. 12) represents a more realistic situation. The initial velocity distribution (Fig. 12, left column) includes several high-velocity anomalies with a shape similar to that of the observed anomalies of the data inversion along the vertical profiles in Fig. 4. This test is aimed at checking the capacity of the algorithm to provide stable imaging for the hypotheses concerning the slab interaction under the Pamir–Hindukush regions (Section 4.1). As in the first test, noise with a standard deviation of 0.5 s and 10 per cent of outliers is added (noise + outliers give a standard deviation 0.95 s). In this case the inversion procedure also includes the step of absolute source location and rejection of outliers. The results for the *P* and *S* models presented in Fig. 12 (middle and right columns, correspondingly) show a stable reconstruction of all significant features observed in the real data inversion. This test shows the capacity of the algorithm to resolve a complicated scenario of lithospheric plate interaction. Both synthetic tests show that for the *S* model the quality of reconstruction is not significantly worse than for the *P* model, in contrast to the significant difference in the real data inversion. This means that the *S* model smearing observed in the real data inversion is mostly due to noise, which is higher than in the test, and not due to insufficient *S* ray coverage.

5 SUMMARY AND DISCUSSION

In this work we have extended the ITS (Koulakov 1998; Koulakov *et al.* 2002) and applied it to the Pamir–Hindukush region. The resulting images of velocity anomalies beneath the Pamir–Hindukush and surrounding areas show a rather complicated shape of the subducting slab in the collision zone of the Asian and Indian plates. With our tomographic images, we show that under Western and Central Hindukush, the Indian plate subducts northwards under the Asian plate. Under the Pamir, the Indian plate overturns and begins to subduct southwards. The corresponding shape of the slab is corroborated by the distribution of relocated deep sources and is consistent with several previous studies (Billington *et al.* 1977; Vinnik *et al.* 1977; Pegler & Das 1998; van der Voo *et al.* 1999; Pavlis & Das 2000). An overturned Indian plate beneath Pamir is also consistent with the counter-clockwise rotation of the India (e.g. Replumaz & Tapponnier 2003) and the idea of simple mantle shear flow by Pavlis & Das (2000). However, the subducting plate does not look like the hanging remnant of the oceanic crust, as reported by Pavlis & Das (2000). Instead it has a clear continuation to at least the bottom of the mantle transition zone. Between 71–73°E, the slab is strongly deformed and thinned to ∼250 km depth, probably experiencing an *on-going break-off*, which is already completed east of the 74°E. Therefore, according to our interpretation, the Pamir–Hindukush region exhibits a rare (if not unique) case of a currently developing break-off of the huge slab, whose dynamic consequences certainly deserve special investigation.

An interesting question is what is the cause of deep seismicity beneath the Pamir–Hindukush that is characteristic of a subduction? As we have seen from our tomographic images (Figs 4–6), the deep seismicity almost always occurs in the domains of highest velocities. This would be consistent with the idea of the remnant of a cold oceanic slab (Pavlis & Das 2000). However, as mentioned above, the clear continuation of this structure to a depth of more than 600–700 km apparently contradicts this model. Additional arguments against relicts of oceanic lithosphere come from considerations of the geological history of the region. These suggest that there is no oceanic crust of suitable age in the region (Searle *et al.* 2001). Therefore, Searle *et al.* (2001) suggest that the rocks which host the deep seismicity in the Pamir–Hindukush region are eclogitized lower crustal rocks of the India plate.

However, at least the following two reasons argue against the latter model. First, there are no minerals in the lower crustal rocks

containing water deeper than 100 km (3 Gpa) (e.g. Hacker *et al.* 2003). Therefore, no dehydration embrittlement, required to trigger earthquakes at large depth, can occur in such rocks at depths from 100–250 km, where most of the Pamir–Hindukush deep seismicity is located. Secondly, silica oversaturated eclogites that are expected to form after eclogitization of the typical continental lower crustal rocks, have lower seismic velocities than the mantle (Sobolev & Babeyko 1994). It can be shown that with *ca.* 10 per cent of free SiO_2, this still holds even in the coesite stability field. Therefore, the observed coexistence of the highest seismic velocities and deep earthquake clusters (Figs 4 and 9) seems to contradict the idea of a continental crust in the Pamir–Hindukush deep seismogenic zone. From the above discussion it is clear that no suitable explanation of the intriguing deep seismicity in this region is available so far. However, we think that the observed seismic structure and deep seismicity still require the presence of preserved oceanic lithosphere or transitional lithosphere of the Indian plate margin containing thick, cold and partially serpentinized (along faults) mantle lithosphere. Such lithosphere has high seismic velocities, and its dehydration and deformation may trigger seismicity. This lithosphere is still linked to the deeper part of the slab, west of the Tarim margin, acting as a strong edge of the indenting Indian plate. While moving northwards, this lithosphere causes intensive tectonic shortening of the Asian plate, but it is also deforming itself. This deformation, together with the dehydration embrittlement of the mantle lithosphere causes unusually intense seismicity. We speculate that similar lithosphere may have been present in the geological past also further to the east, along the Tarim margin, but it has already been detached due to the collision with the strong lithosphere of the Tarim block. We believe that this particular process is going on now at the western tip of the Tarim lithosphere.

To assess the reliability of our observations and interpretation, and to delineate the resolution power of our algorithm, we conducted a series of synthetic tests adding realistic noise and outliers to synthetic arrival times. The results show that for a region such as the Pamir–Hindukush with its high seismicity, we have satisfactory resolution power of anomalies at both crustal and upper mantle depths.

Finally we conclude that the ITS, powered by built-in precise source relocations, is an efficient technique to image deep seismic structure in remote seismogenic regions with poor coverage by seismic stations.

ACKNOWLEDGMENTS

We are very grateful to Gabi Laske, Gary Pavlis and another anonymous reviewer for their unselfish work and time spent on editing and correcting our manuscript. Thanks to their criticism, we were able to improve significantly our study.

REFERENCES

Bazhenov, M.L. & Burtman, V.S., 1986. Tectonics and peleomagnetism of structural areas of the Pamir-Punjab syntaxis, *J. Geodyn.,* **5,** 383–396.

Bassin, C., Laske, G., Masters, G., Bassin, C., Laske, G. & Masters, G., 2000. The current limits of resolution for surface wave tomography in North America, *EOS, Trans. Am. geophys. Un.,* **81,** F897.

Beloussov, V.V., Pavlenkova, N.I. & Egorkin, A.V., 1991. *Deep Structure of the Territory of the USSR*, Nauka, Moscow p. 224.

Bijwaard, H., Spakman, W. & Engdahl, R., 1998. Closing the gap between regional and global travel time tomography, *J. geophys. Res.,* **103,** 30 055–30 078.

Bijwaard, H. & Spakman, W., 2000. Non-linear global P-wave tomography by iterated linearized inversion, *Geophys. J. Int.,* **141,** 71–82.

Brandon, C. & Romaniwicz, B., 1986. A 'no-lid' zone in the Central Chang-Thang platform of Tibet: evidence from pure path phase velocity measurments of long period Rayleigh waves, *J. geophys. Res.,* **91,** 6547–6564.

Billington, S., Isacks, B.I. & Barazangi, M., 1977. Spacial and focal mechanisms of mantle earthquakes in the Hindu Kush–Pamir region: a contorted Benioff zone, *Geology,* **5,** 699–704.

Blundell, D., Freeman, R. & Mueller, St., eds, 1992. *A Continent Revealed: the European Geotraverse*, Cambridge Univ. Press, Cambridge, p. 276.

Burov, E.V., Kogan, M.J., Lyon-Caen, H. & Molnar, P., 1990. Gravity anomalies, the deep structure, and dynamic process beneath the Tien Shan, *Earth planet. Chi. Lett.,* **96,** 367–383.

Burtman, V.S. & Molnar, P., 1993. Geological and geophysical evidence for deep subduction of continental crust beneath the Pamir, Geological Society of America Special Paper 281, p. 76.

Chatelin, J.L., Roecker, S.W., Hatzfeld, D. & Molnar, P., 1980. Microearthquake seismicity and fault plane solutions in the HinduKush region and their tectonic implications, *J. geophys. Res.,* **85,** 1365–1387.

De Mets, C., Gordon, R.G., Argus, D.F. & Stein, S., 1994. Effects of recent revision to the geomagnetic reversal time scale on estimates of current plate motions, *Geophys. Res. Lett.,* **21,** 2191–2194.

Fan, G., Ni, J.F. & Wallace, T.C., 1994. Active tectonics of the Pamirs and Karakorum, *J. geophys. Res.,* **99,** 7131–7160.

Hacker, B.R., Abers, G.A. & Peacock, S.M., 2003. Subduction Factory 1. Theoretical mineralogy, densities, seismic wave speeds, and H_2O contents, *J. geophys. Res.,* **108,** doi: 10.1029/2001JB001127.

Hamburger, M.W., Sarewitz, D.R., Palvis, T.L. & Popandopulo, G.A., 1992. Structural and seismic evidence for intracontinental subduction in the Peter the First Range, central Asia, *Geol. Soc. Am. Bull.,* **104,** 397–408.

International Seismological Centre, 2001. Bulletin Disks 1–9 [CD-ROM], Internatl. Seis. Cent., Thatcham, UK.

Kennett, B.L.N., Engdahl, E.R. & Buland, R., 1995. Constraints on seismic velocities in the Earth from traveltimes, *Geophys. J. Int.,* **122,** 108–124.

Koulakov, I., 1998. Three-dimensional seismic structure of the upper mantle beneath the central part of the Eurasian continent, *Geophys. J. Int.,* **133,** 467–489.

Koulakov, I., Tychkov, S., Bushenkova, N. & Vasilevskiy, A., 2002. Structure and dynamics ovf the upper mantle beneath the Alpine-Himalayan orogenic belt, from teleseismic tomography, *Tectonophys,* **358,** 77–96.

Li, S. & Mooney, W.D., 1998. Crustal structure of China from deep seismic sounding profiles, *Tectonophysics,* **288**(1–4), 30, 105–113.

Lukk, A.A. & Vinnik, L.P., 1975. Tectonic Interpretation of the Deep Structure of the Pamirs,, *Geotektonika,* **10**(5), 73–80.

Maggi, A., Jackson, J.A., Priestley, K. & Baker, C., 2000. A re-assessmentof focal depth distributions in southern Iran, the Tien Shan and northern India: do earthquakes really occur in the continental mantle?, *Geophys. J. Int.,* **143,** 629–661.

Meissner, R., Wever, T. & Fluh, E.R., 1987. The Moho in Europe—implications for crustal development, *Annales-Geophysicae, Series B.,* **5B**(4), 357–364.

Molnar, P., 1988. A review of geophysical constraints on the deep structure of the Tibetan plateau, the Himalaya, and the Karakorum and their tectonic implications, *Phil. Trans. Roy. Soc. London, ser. A.,* **326,** 33–88.

Mooney, W.D., Laske, G. & Masters, T.G., 1998. CRUST 5.1: a global crustal model at 5 × 5, *J. geophys. Res.,* **103,** 727–747.

Paige, C.C. & Saunders, M.A., 1982. LSQR: An algorithm for sparse linear equations and sparse least squares, *ACM trans. Math. Soft.,* **8**(5), 43–71.

Pavlis, G.L. & Das, S., 2000. The Pamir-Hindu Kush seismic zone as a strain marker for flow in the upper mantle, *Tectonics,* **19,** 103–115.

Pavlis, G.L. & Booker, J.R., 1980. The mixed Discrete-Continuous inverse problem: application to the simultaneous Determination of earthquake hypocenters and velocity structure, *J. geophys. Res.,* **85,** 4801–4810.

Pegler, G. & Das, S., 1998. An enhanced image of the Pamir-Hindu Kush seismic zone from relocated earthquake hypocenters, *Geophys. J. Int.,* **134,** 573–595.

Replumaz, A., Karason, H., van der Hilst, R.D., Besse, J. & Tapponnier, P., 2004. 4-D evolution of SE Asia's mantle from geological reconstructions and seismic tomography, *Earth planet. Sci. Lett.,* **221,** 103–115.

Replumaz, A. & Tapponnier, P., 2003. Reconstruction of the deformed collision zone between India and Asia by backward motion of lithospheric blocks, *J. geophys. Res.,* **108**(B6), 2285, doi:10.1029/2001JB000661.

Robinson, A.C., Yin, A., Manning, C.E., Harrison, T.M., S.-H. Zhang, & X.-F. Wang, 2004. Tectonic evolution of the northeastern Pamir: constraints from the northern portion of the Cenozoic Kongur Shan extensional system, western China, *GSA Bulletin,* **116**(7/8), 953–973.

Roecker, S.W., 1982. Velocity structure of the Pamir–Hindu Kush region: possible evidence of subducted crust, *J. geophys. Res.,* **87,** 945–959.

Searle, M., Hacker, B.R. & Bilham, R., 2001. The Hindu Kush seismic zone as a paradigm for the creation of ultrahigh-pressure diamond and coesite-bearing rocks. *J. Geol.,* **109,** 143–154.

Seber, D., Vallve, M., Sandvol, E., Steer, D. & Barazangi, M., 1997. Middle East Tectonics: applications of geographic information system (GIS), *GSA Today,* **7,** 1–6.

Sobolev, S.V. & Babeyko, A., 1994. Modeling of mineralogical composition and elastic wave velocities in anhydrous magmatic rocks, *Surv. Geophys.,* **15,** 515–544.

Sobolev, S.V., Zeyen, H., Stoll, G., Werling, F., Altherr, R. & Fuchs, K., 1996. Upper mantle temperatures from teleseismic tomography of French Massif Central including effects of composition, mineral reactions, anharmonicity, anelasticity and partial melt, *Earth planet. Sci. Lett,* **139,** 147–163.

Sobolev, S.V., Zeyen, H., Granet, M., Achauer, U., Bauer, C., Werling, F., Altherr, R. & Fuchs, K., 1997. Upper mantle temperature and lithosphere-asthenosphere system beneath the French Massif Central constrained by seismic, gravity, petrologic and thermal observations, *Tectonophys.,* **275,** 143–164.

van der Sluis, A. & van der Vorst, H.A., 1987. Numerical solution of large, sparse linear algebraic systems arising from tomographic problems, in *Seismic tomography*, pp. 49–83, ed. Nolet, G., Reidel, Dortrech.

van der Voo, R., Spakman, W., Bijwaard, H., 1999. Tethyan subducted slabs under India, *Earth planet. Sci. Lett.,* **171,** 7–20.

Vinnik, L.P., Lukk, A.A. & Nersesov, I.L., 1977. Nature of the intermediate seismic zone in the mantle of the Pamir-Hindu Kush, *Tectonophysics,* **38,** 9–14.

Vinnik, L.P., Reigber, C., Aleshin, I.M., Kosarev, G.L., Kaban, M.K., Oreshin, S.I. & Roecker, S.W., 2004. Receiver function tomography of the central Tien Shan, *Earth planet, Sci. Lett.,* **225,** 131–146.

Waldhauser, F. & Ellsworth, W., 2000. A double-difference Earthquake location algorithm: method and application to the northern Hayward fault, California, *Bull. seism. Soc. Am.,* **90**(6), 1353–1368.

Wittlinger, G. *et al.*, 2004. Teleseismic imaging of subducting lithosphere and Moho offsets beneath western Tibet, *Earth planet. Sci. Lett.,* **221,** 117–130.

Ziegler, P.A., 1990. Geological Atlas of Western and Central Europe. Shell Internat. Petrol. Mij. and Geol. Soc., London, p. 239 and 56 encl.

Zonenshain, L.P., Kuzmin, M.I. & Natapov, L.M., 1990. Geology if the USSR: A Plate-Tectonic Synthesis, in *Geodyn. Ser.*, Vol. 21, p. 242, ed. Page, B.M., AGU, Washington, DC.

APPENDIX A: ALGORITHM OF ABSOLUTE SOURCE LOCATION

The algorithm of absolute source location is based on minimization of the observed traveltime residuals. The residual times for the location, dt_{ij}, are computed iteratively. At the Nth iteration,

$$dt_{ij}^{N} = dt_{ij}^{N-1} - \left\{ \sum_{j=1}^{M_i^{N-1}} A(\Delta_{ij})\, dt_{ij}^{N-1} \right\} \Big/ M_i^{N-1}, \tag{A1}$$

where M_i^{N-1} is the number of 'good' observations (i.e. observations with residuals less than a predefined value; $dt^{\max}$) and $A(\Delta_{ij})$ is a weight function depending on the distance between the source and the receiver. It is assumed that the short rays accumulate smaller residuals than the long ones; hence they are given greater weights for the determination of the origin time.

In the first iteration,

$$dt_{ij}^{0} = t_{ij}^{\text{obs}} - t_{ij}^{\text{ref}} \quad \text{and} \quad M_i^0 = M_i, \tag{A2}$$

where t_{ij}^{obs} is the observed and t_{ij}^{ref} is the reference traveltime between the ith source and the jth station. M is the total number of recorded phases for the ith source. The maximal residual among all phases is identified. If it is greater than a predefined value ($dt_{\max}$), it is considered as an outlier and is rejected. Consequently, all the residual times are computed anew and the procedure of identification and rejection of outliers is repeated until all the remaining residuals are less than $dt_{\max}$.

If the earthquake is deep and pP and sS phases are recorded, they play an important role in the determination of the source depth. The residual times in this case are written as:

$$\begin{aligned} \Delta t^{pP-P} &= \left(t_{\text{obs}}^{pP} - t_{\text{obs}}^{P}\right) - \left(t_{\text{ref}}^{pP} - t_{\text{ref}}^{P}\right) \\ \Delta t^{sS-S} &= \left(t_{\text{obs}}^{sS} - t_{\text{obs}}^{S}\right) - \left(t_{\text{ref}}^{sS} - t_{\text{ref}}\right). \end{aligned} \tag{A3}$$

During the source location these picks appear with greater weights.

To find the source coordinates and the origin time, it is necessary to define the probability function of a source existing at any point of the study area. Here we propose two criteria. The primary criterion is the number of 'good' observations, meaning those observations with residuals less than a predefined value: $dt^{\max}$. The second criterion is the value of the goal function which is defined as:

$$G = \sum_{j=1}^{M^{\text{good}}} \| B_j W_j(d)\, dt_j \| \Big/ \sum_{j=1}^{M^{\text{good}}} \| B_j W_j(d) \|, \tag{A4}$$

where double parenthesis mean L2 norm, dt_{ij} is the residual measured for the i source at the j station, M_{good} is the number of good observations, B is a weight depending on the phase type (P is 1, S is 0.7, Pp or Ss is 3) and $W(d)$ is the weight depending on epicentral distance. For distances up to 50 km it is assigned 1, and in the interval between 50 and 600 km it linearly decreases the value from 1 to 0.1; for the greater distances the value remains constant of 0.1.

The preliminary position of a source is determined by searching on a regular grid constructed around the location reported in the initial catalogue (ISC). The lateral size of the grid is 100 km with nodes placed at 10 km intervals. Of the nodes with maximum numbers of 'good' residuals we select one where the goal function has the minimum value. From the selected node, components of the direction vector (dx, dy, dz) along which the goal function decreases more rapidly are determined by solving the standard location equations:

$$P_i^x\, dx + P_i^y\, dy + P_i^z\, dz + dt^0 = dt_i \quad i = 1 \ldots M^{\text{good}}. \tag{A5}$$

where P_i is the slowness vector of the ith ray at the source point. This system is solved by the least square method. If the number of 'good' observations at the next point is greater than at the previous point, or when it remains unchanged whereas the value of the goal function becomes smaller, we move to the next point. Otherwise, the midpoint of the direction vector is taken as the next point. The procedure continues from there until a point is reached from which the minimal step displacement in any direction leads to a greater value of the goal function.